VNU Journal of Science: Earth and Environmental Sciences, Vol. 42, No. 3 (2026) 57-68

VNU Journal of Science: Earth and Environmental Sciences

Journal homepage: https://js.vnu.edu.vn/EES

Original Article

Integrating Sentinel-1 Insar Coherence and Sentinel-2 Imagery for Detecting Built-up Features in the Hanoi Area

Le Minh Hang, Vu Van Truong*, Ho Duc Hung

Le Quy Don Technical University, 236 Hoang Quoc Viet, Hanoi, Vietnam

Received 26th July 2025
Revised 17th January 2026; Accepted 5th March 2026

Abstract: Remote sensing has been applied to rapidly and accurately determine information about surface land cover, including urban areas. There are two urban land covers in the Hanoi area: i) Densely populated with little urban vegetation cover in the central Hanoi; and ii) Less densely populated with greenery dispersion in the suburban Hanoi. Buildings typically have a higher InSAR coherence value on microwave satellite imaging than other objects due to their fixed nature. Based on the urban features of the Hanoi region, we suggested an approach for classifying urban elements by integrating the InSAR coherence map of the two polarizations, VV and VH, from Sentinel-1 with the spectral index imagery UI and CI from Sentinel-2. To improve the automation of the classification, we tested the unsupervised K-means classification method on two groups: urban and non-urban. The classification results achieved an accuracy of 78.8% for the case using the InSAR correlation imagery (VV and VH polarizations), 88% for the case using the spectral index images (UI and CI), and 92.1% for the case combining the InSAR correlation and spectral index images. Nonetheless, there was still considerable misinterpretation and noises in the classification results, especially with asphalt roads and river sand. The results demonstrate that combining Sentinel-1 and Sentinel-2 enhances the ability to detect built-up features and supports more effective large-scale land cover monitoring.

Keywords: Coherence mapping, spectral soil indices, integrating data, Sentinel-1, Sentinel-2.

1. Introduction

Accurate and timely mapping of built-up areas plays an essential role in Earth observation and urban monitoring applications [1]. Built-up objects (urban objects) include impermeable surfaces, roads, and buildings in residential areas. The expansion of urban areas can lead to

* Corresponding author.
E-mail address: truongvv@lqdtu.edu.vn

https://doi.org/10.25073/2588-1094/vnuees.5329

significant environmental consequences, such as the loss of green spaces, increased concrete coverage, the formation of urban heat islands, elevated air pollution, flooding, waterlogging, and other issues [2]. The Hanoi Statistical Yearbook states that in 2019, Hanoi's land area consisted of 40.0% non-agricultural land and 58.3% agricultural land [3]. By 2024, the agricultural land area in Hanoi was 58.5%, and non-agricultural land was 40.7% [4]. The overall land use situation in Hanoi hasn't changed much between 2019 and 2024. However, an analysis of the percentage share of urban residential land and rural residential land reveals a significant change within the composition of non-agricultural land. The urban residential land in Hanoi was 3.5% in 2019 [3] and 8.6% in 2024 [4], while the corresponding rural residential land was 8.7% [3] and 3.3% [4], respectively. The average population growth rate in Hanoi is 1.5% [4]. Thus, the annual population increase has led to growth in urban residential land in Hanoi. Therefore, it is necessary to monitor and update the urban land area annually, especially in major cities like Hanoi.

Currently, urban areas are updated annually based on multiple data sources, including remote sensing data. The Earth's surface is observed using remote sensing technologies based on various spectral bands. Two commonly used types of remote sensing data for land cover classification are optical and microwave imagery [5]. Spectral bands in optical images and backscatter signals in SAR (SAR-Synthetic Aperture Radar) images provide complementary information for identifying land cover features. However, differences in wavelength characteristics, environmental influences, and sensor-specific image properties can lead to classification errors. Optical satellites function by detecting reflected solar radiation from the Earth's surface, a method of passive remote sensing [7]. In addition to having a high spatial resolution, they provide a lot of information regarding spectral and textural characteristics. However, the environment and available light levels can influence them. Microwave satellites are active sensors that utilize microwave frequencies to penetrate clouds, enabling the collection of data in all weather conditions and at any time of day [8]. Nevertheless, SAR imagery frequently exhibits speckle noise and a lower signal-to-noise ratio. Due to these limitations on the information that can be acquired, it is impossible for a single image source to accurately, consistently, and comprehensively represent the true state of land cover features. Consequently, it is imperative to effectively integrate data from both optical and SAR imagery [11].

The goal of multi-source data integration is to preserve the unique attributes of each data type while minimizing discrepancies between them [14]. Structural consistency between optical and SAR images, particularly with multi-source and multi-polarization SAR data, is often exploited during integration, as image structure remains stable regardless of sensor mode and is not affected by noise, illumination, or environmental conditions [17]. The integration of satellite imagery from multiple sources can be categorized into three approaches: i) Pixel-based integration; ii) Decision integration; and iii) Object-based integration [19]. The pixel-based integration method performs an in-depth analysis of individual pixels from several sources of imagery. This strategy ensures minimal information loss. Nevertheless, it has significant memory and equipment requirements and analyzes a lot of data. The approach of decision-level integration is dependent on the classification results obtained from each image source and employs a variety of criteria to arrive at a variety of results. This method provides quick computational speed and requires little precision when registering images from various data sources. Classifying object information from the original images is part of the object-based integration method. This step is followed by the processing of the objects themselves, which results in the classification, linking, and integration of several sources of images of the same scene. This approach has the capacity to compress information, reduce data size, and

analyze and integrate features from various data types in a variety of ways [20].

In the paper, the authors present experimental results using the pixel-based integration method, which include Interferometric Synthetic Aperture Radar (InSAR) cohenrence maps from the Sentinel-1 satellite and spectral soil index imagery from the Sentinel-2 satellite for the purpose of urban classification.

2. The Study Area and Materials

2.1. The Study Area

The study area is Hanoi City, Vietnam (Figure 1a). Hanoi is in the center of the Red River Delta and functions as the principal transportation intersection as well as the political, economic, and cultural epicenter of the nation, serving as an essential connection among the country's regions [21].

The landscape progressively descends from north to south and from west to east, with an average elevation of between 5 and 20 meters above sea level. The delta region comprises approximately seventy-five percent of the city's natural land area, located on the right bank of the Đà River and bordering both sides of the Red River, created by alluvial deposits. Hills and mountains are predominantly located in the North and West, particularly the Ba Vì mountain range, which features a peak reaching roughly 1,281 meters, along with the hilly areas of Soc Son and My Duc.

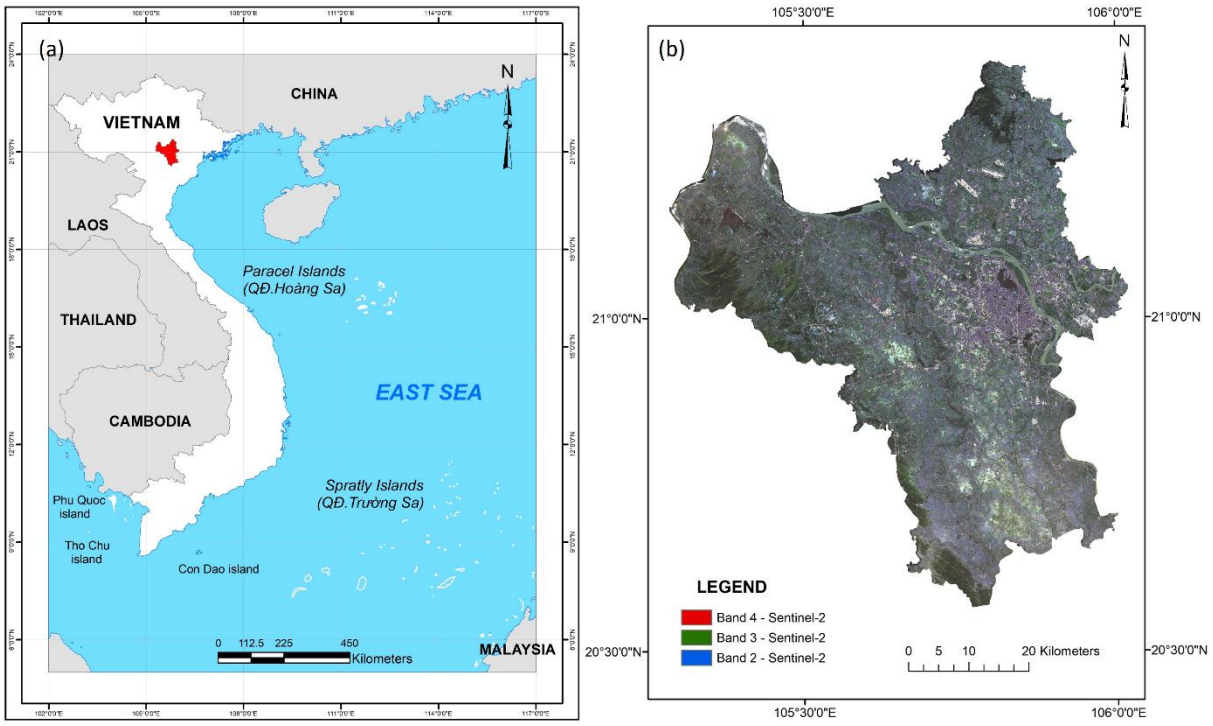


Figure 1. Location of the study area. (a) Geographic location in Hanoi, Vietnam; (b) Natural color composite image from Sentinel-2, acquired on 11 May 2019.

Hanoi's hydrological system comprises numerous principal rivers, including the Hong (Red) River, Da River, Duong River, Nhue River, Cau River, Day River, and Ca Lo River, alongside a network of lakes such as West Lake, Hoan Kiem Lake, and Truc Bach Lake [22].

The predominant soil characteristics in the Hanoi area comprise two main groups: alluvial

soil (accounting for much of the delta area) and ferralsol (occupying most of the hilly and mountainous regions). The alluvial soil is further subdivided into extra-dike alluvial soil (areas receiving annual alluvial deposits) and intra-dike alluvial soil (older, non-annually flooded alluvial deposits). Ferralsol (often referred to as red-yellow soil) is formed through the accumulation of iron and aluminum oxides and is primarily concentrated in the western and northern parts of the city, specifically in districts such as Ba Vi, Soc Son, and Thach That [23].

The study concentrates on classifying urban land objects in Hanoi in 2019 [3]. Statistical data from the Hanoi Statistical Yearbook 2019 confirms the significant proportion of residential land within the city's inner districts [3]. These figures demonstrate that residential land accounts for a large portion of the total area in each of these inner-city zones. Furthermore, compared to 2018, the residential land area saw a sharp increase in certain peripheral areas such as Long Bien, Nam Tu Liem, and Me Linh [3]. In addition to residential areas, specialized land also constitutes a substantial percentage of total non-agricultural land. Specialized land encompasses areas designated for government agencies, national defense and security, non-agricultural production and business, and public purposes. In 2019, specialized land made up 19.1% of all non-agricultural land [3]. Therefore, updating the area of urban land is of crucial importance for monitoring changes in surface cover and the current status of land use in Hanoi.

2.2. Materials

Table 1 presents the characteristics of experimental data. Sentinel-1 data were pre-processed and used to generate InSAR coherence maps using the SNAP Toolbox. Based on the geographic coverage illustrated in the Sentinel-1 imagery metadata (Figure 2), the Hanoi study area is located within sub-swath IW2, specifically covering bursts 1-6 of the first image (acquisition track T110642) and bursts 9-10 of the second image (acquisition track T110549). The Copernicus release states that the Sentinel-1A satellite is affecting the thruster responsible for orbit inclination control, resulting in a change in the orbit inclination of Sentinel-1A starting in mid-April 2024 [24]. Consequently, to guarantee steady data in the InSAR, the author decided to use the 2019 images.

All Sentinel-2 images used in this study were at Level-2A, in which digital number (DN) values were converted to surface reflectance. Sentinel-2 imagery was further processed using the Google Earth Engine (GEE) platform. Both Sentinel-1 and Sentinel-2 images were reprojected to the UTM/WGS-84 coordinate system in zone 48N, clipped to the administrative boundary of Hanoi, and resampled to a common spatial resolution of 10 meters.

Table 1. Characteristics of the materials

Characteristics	Satellite information
Sentinel-1 Satellite	
Acquisition time	05/11/2019; 17/11/2019
Level	SLC (Single-Look Complex)
Polarization	VV and VH
Resolution	10 m
Sentinel-2A Satellite	
Acquistion time	05/11/2019
Level	Level-2A
Bands	2, 3,4,5,8, 11, 12
Resolution	10 m

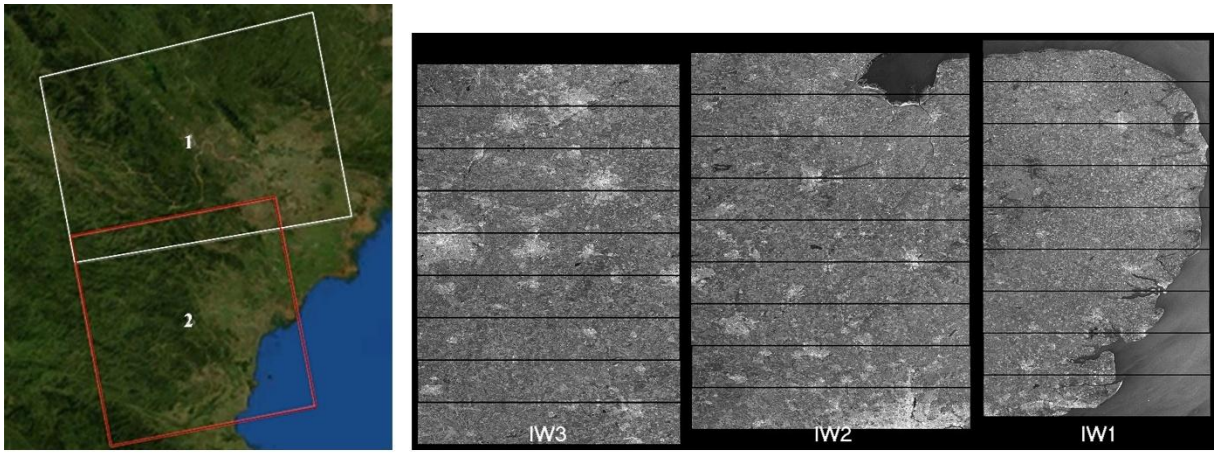


Figure 2. (a) Location of Sentinel-1 with (1) track T110642 and (2) track T110549; (b) IW SLC Bursts and Sub-Swaths of Sentinel-1 [25].

3. Methodology

3.1. Determining Coherence Mapping in InSAR

InSAR coherence is a measure of the quality of the interferometric signal between two SAR images acquired at different times. The coherence value in an InSAR image reflects the degree of similarity in the radar backscatter signals from the same ground location in both acquisitions. Higher coherence values typically correspond to the backsscattering characteristics of the surface changing little or not at all between the two imaging times, such as bare land or urban areas. In this situation, the phase of the radar signal is preserved. In contrast, lower coherence values are generally observed in areas experiencing surface dynamics or signal decorrelation, including vegetation, water bodies, or regions affected by human activities.

The coherence value is calculated using the following equation [26]:

$$\gamma = \frac{E\left\langle s_1 s_2^* \right\rangle}{\sqrt{E\left\langle \left|s_1\right|^2 \right\rangle \cdot E\left\langle \left|s_2\right|^2 \right\rangle}} \quad (1)$$

Where: s_1, s_2 is the corresponding signals on two complex-value SAR images; Symbol $(^*)$ denotes complex operators; The symbol $E\langle . \rangle$ denotes mathematical expectation [27].

The coherence value in formula (1) quantifies the average coherence between s_1, s_2 two corresponding images. It encodes the degree of coherence as a value within the range [0, 1].

Several factors influence the coherence value between two images in InSAR:

- SAR system noise: Interference from signal noise within the SAR image acquisition system can degrade coherence.
- Misregistration: Loss of coherence can occur during the image co-registration process between the master and slave images.
- Geometric decorrelation: Differences in viewing geometry or baseline length between image acquisitions can cause pixel misalignment. A shorter baseline reduces geometric decorrelation.
- Volume scattering: Caused by the scattering of radar signals within a medium (e.g., vegetation), volume scattering leads to reduced coherence. It is strongly influenced by radar wavelength and the dielectric properties of the target surface. For example, dense vegetation or forested areas typically exhibit strong volume scattering.

- Temporal decorrelation: Refers to surface changes over time that alter the radar signal, including both geometric and electrical property changes. These are mainly due to vegetation dynamics, surface erosion, or human activity. Temporal decorrelation is strongly dependent on the radar system's operating frequency [27].

The effects of signal noise, image co-registration, or baseline length can be eliminated if the satellite's geometric conditions are ensured and interferometric processing steps are performed accurately [28]. Therefore, detecting surface changes requires careful assessment and analysis of the coherence image.

In practical applications, it is essential to achieve high contrast in the coherence image between changed and unchanged areas. To enhance this contrast, the coherence value is redefined using the following formula:

$$\gamma' = \frac{\left|\sum_{i=1}^{N} s_{1,i} \cdot s_{2,i}^{*} . e^{j\phi(i)}\right|}{\sqrt{\sum_{i=1}^{N}\left|s_{1,i}\right|^2 \sum_{i=1}^{N}\left|s_{2,i}\right|^2}} \quad (2)$$

Where: i is the ith pixel in the window with a total of N pixels. Correlation Values γ' which is biased due to the correlation of the signal $\phi(i)$ presented in the interference phase. This component of the phase contains the influence of photographic geometry, terrain, and motion [29].

3.2. Determination of Built-up Indices Using Sentinel-2 Imagery

The Sentinel-2 satellite is an optical Earth observation platform that is part of the Copernicus Programme, jointly operated by the European Commission and the European Space Agency (ESA). Sentinel-2 provides 13 spectral bands, including visible and shortwave infrared (SWIR) bands at 20 m spatial resolution, as well as atmospheric correction bands at 60 m resolution [30]. In this study, several remote sensing indices are employed to detect built-up areas, including the Urban Index (UI) and Colour Index (CI).

The UI is a remote sensing index developed to identify built-up areas (or urban land objects). The original UI was proposed for Landsat imagery (utilizing Band 7 and Band 4) and is defined by the following formula [30]:

$$UI = \frac{SWIR2 - NIR}{SWIR2 + NIR} \quad (3)$$

Where: SWIR2 is the surface reflectance value of the Shortwave-infrared band (Band 7 in Landsat TM/ETM+); NIR is the surface reflectance value of the Near-infrared band (Band 4 in Landsat TM/ETM+).

For the Sentinel-2 satellite, the SWIR2 band equivalent corresponds to Band 12, which has a wavelength range of 2100–2280 nm [30]. The NIR band equivalent corresponds to Band 8, which has a wavelength range of 758–899 nm [30]. The UI is formulated based on the spectral contrast between built-up areas and vegetation. The UI values range from [-1, 1]. Specifically, values approaching +1 correspond to built-up (or urban) objects. Low values, which approximate -1, correspond to vegetation or water bodies. The materials, such as concrete, asphalt, and buildings, exhibit strong reflectance in the SWIR2 wavelength range and weak reflectance in the NIR wavelength range. Consequently, the UI value for urban objects is consistently positive and high. Conversely, vegetation typically displays low reflectance in the SWIR2 range and very strong reflectance in the NIR range. Therefore, vegetation objects generally possess negative UI values. Water bodies absorb nearly all energy in both the NIR and SWIR2 wavelengths; thus, the UI value for water is typically low and also negative.

The classification of urban land objects using the UI image is fundamentally based on these distinctive spectral reflectance characteristics across the relevant wavelengths. The UI is conceptually similar to the Normalized Difference Built-up Index (NDBI), which was proposed by Zha et al., (2003) [31] and expresses the relationship between the NIR and SWIR1 bands.

The CI was developed by Pouget et al., (1991) [32]. The CI was designed to differentiate

between different soil types based on their spectral reflectance characteristics. Factors such as mineral content, organic matter, and soil moisture will create differences in CI images. The formula for determining CI is as follows:

$$CI = \frac{RED - GREEN}{RED + GREEN} \quad (5)$$

Where: RED is the surface reflectance of RED band; GREEN is the surface reflectance of GREEN band.

The CI is a spectral index designed to differentiate various types of bare soil, particularly surfaces with distinct color variations typical of arid regions [32].

For built-up surfaces, reflectance is typically high in both the RED and GREEN bands compared to vegetation. The spectral curve of construction materials (impervious surfaces) is generally flatter than that of bare soil, resulting in a less significant difference between the RED and GREEN band reflectance. Consequently, the CI values for built-up areas tend to be moderate or slightly positive (depending on the material's specific color composition, such as red roofs or grey concrete).

Bare soil (dry, non-vegetated ground) demonstrates significant distinctions from iron-oxide-rich soil and carbonate/sulfate-rich soil. Iron-oxide-rich soil (red soil) exhibits greater RED reflectance compared to GREEN reflectance, resulting in a high positive CI value. The green reflectance of the carbonate/sulfate-rich soil (bright/white soil) is almost equivalent to its red reflectance, yielding a low CI value (close to 0 or slightly negative). The CI can also indirectly assist in distinguishing urban areas from surroundings.

3.3. The Proposed Method

Urban regions in Hanoi can be broadly divided into two categories. The central area is highly urbanized, where natural vegetation has largely been replaced by concrete structures and residential buildings. As a result, there is a limited presence of green spaces such as urban trees and public parks. In contrast, suburban areas generally contain more vegetation and scattered bare surfaces interspersed within built-up regions. These differences in land cover create challenges in distinguishing urban from non-urban areas, particularly when spectral characteristics of urban features and bare soils partially overlap.

To address this issue, the authors propose an integrated approach for extraction of urban land by combining Sentinel-1 and Sentinel-2 imagery, as illustrated in Figure 3. The integration process merges InSAR coherence maps (VV and VH polarizations) from Sentinel-1 with selected spectral indices (UI and CI) from Sentinel-2 into a unified multi-band dataset. This integration enhances the separability of urban features by exploiting both backscatter stability and spectral characteristics.

For the classification phase, an unsupervised K-means clustering algorithm is applied to the integrated dataset. In this method, pixels are grouped based on the similarity of their spectral and coherence values properties across multiple bands. Unlike supervised approaches, K-means automatically identifies natural data clusters without requiring pre-labeled samples. The algorithm iteratively calculates the Euclidean distance between each pixel and the cluster centroids, updating these centroids until convergence is achieved. In this study, two classes were defined - urban and non-urban. The K-means algorithm is well-suited for large-scale remote sensing datasets due to its simplicity, robustness, and computational efficiency, making it appropriate for automatic urban feature extraction in heterogeneous environments like Hanoi.

The workflow illustrated in Figure 3 is implemented using the SNAP Toolbox software and consists of four main processing stages:

- Part 1. Sentinel-1 image processing

This stage involves processing Sentinel-1 SAR data acquired at two different times to generate the InSAR coherence map. Both VV and VH polarizations are utilized to capture structural and temporal characteristics of the surface.

- Part 2. Sentinel-2 image collection and pre-processing

Sentinel-2 optical imagery is obtained from the Google Earth Engine (GEE) platform and preprocessed to Level-2A. At this level, the Digital Number (DN) values represent surface reflectance. Only images with cloud coverless than 10% are selected. The images are then clipped to match the boundary of the study area. Calculate the UI and CI index on the Sentinel-2 image.

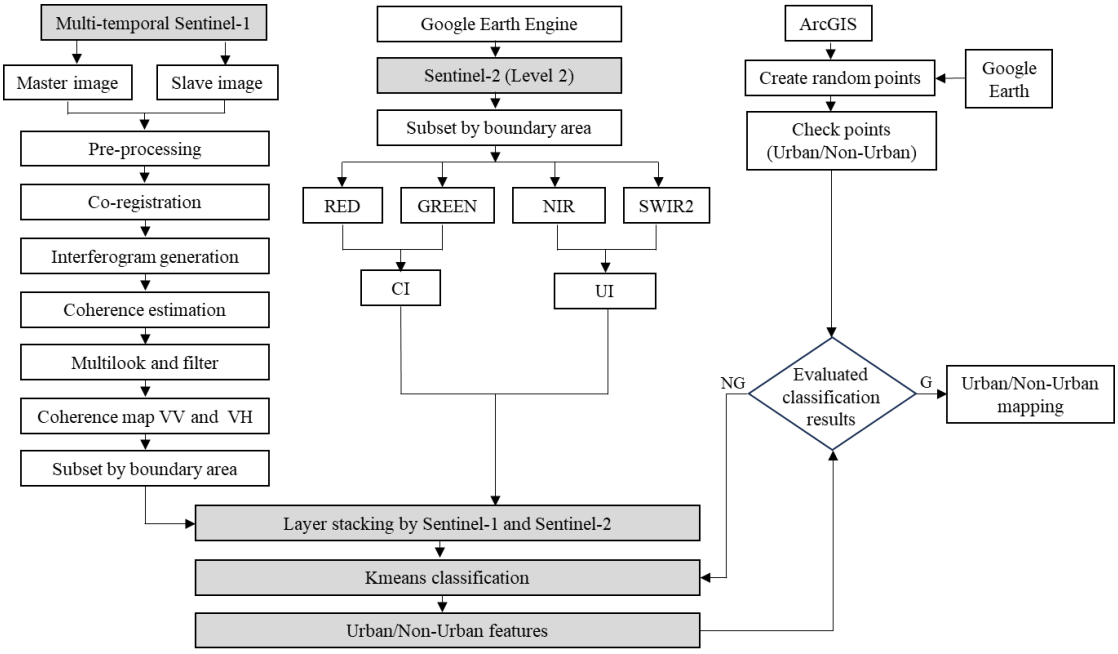


Figure 3. Sentinel-1 and Sentinel-2 data integration process for extracting urban land features.

- Part 3. Data integration and unsupervised classification

This step stacking the coherence maps (VV and VH) from Sentinel-1 with the built-up indices (UI, CI) derived from Sentinel-2 imagery. The combined dataset is subjected to unsupervised classification using the K-means algorithm to differentiate between urban and non-urban areas. Urban features are labeled with a value of 1, while non-urban features are assigned a value of 0.

- Part 4. Accuracy Assessment

After the unsupervised classification, an accurate assessment is conducted to evaluate the reliability of the extracted urban features. Based on this evaluation, a decision rule is applied, as illustrated in Figure 3, to determine whether the classification outcome is acceptable (G – Good) or requires further improvement (NG – Not Good). If the classification performance satisfies the predefined accuracy requirements (G), the resulting urban map is finalized and exported. Otherwise (NG), an iterative refinement process is applied. In this process, key parameters of the K-means clustering algorithm, such as the maximum number of iterations and centroid initialization, are adjusted, and the classification is re-executed. This iterative procedure enables better convergence and more stable clustering results, thereby improving the separability between urban and non-urban classes. The refinement cycle is repeated until an acceptable level of classification accuracy is achieved, ensuring the robustness and consistency of the proposed integrated Sentinel-1 and Sentinel-2 approach.

The final assessment is performed by comparing the classification results with

reference data to quantify the accuracy and reliability of the proposed method. This evaluation is conducted for different experimental scenarios defined by various combinations of Sentinel-1 and Sentinel-2 input features. These scenarios are designed to analyze the individual contribution of each data source as well as the added value of their integration. The detailed description of the experimental scenarios and the corresponding classification results are presented and discussed in Section 4.

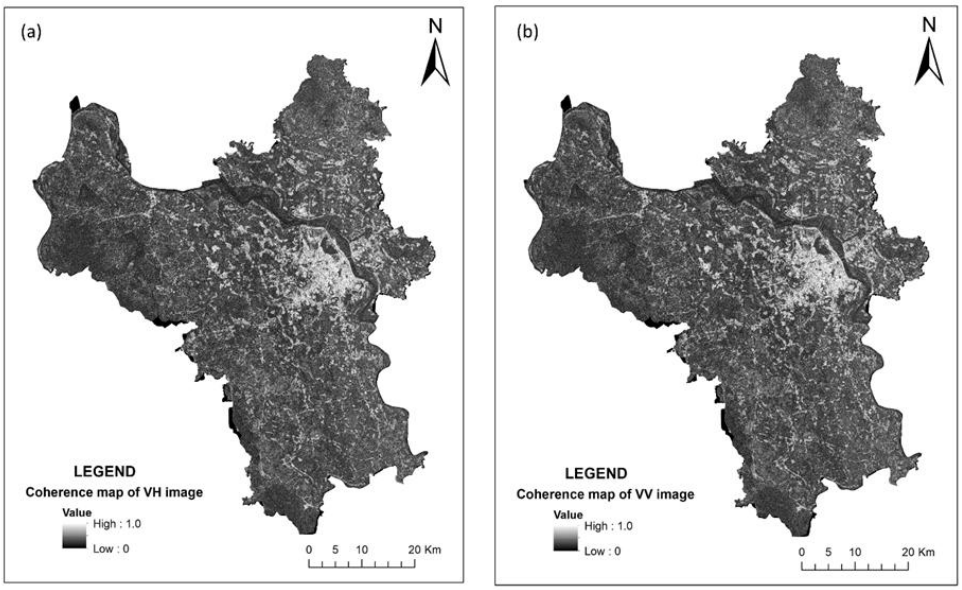


Figure 4. Coherence mapping by Sentinel-1 imagery: (a) VH polarization coherence mapping; (b) VV polarization coherence mapping.

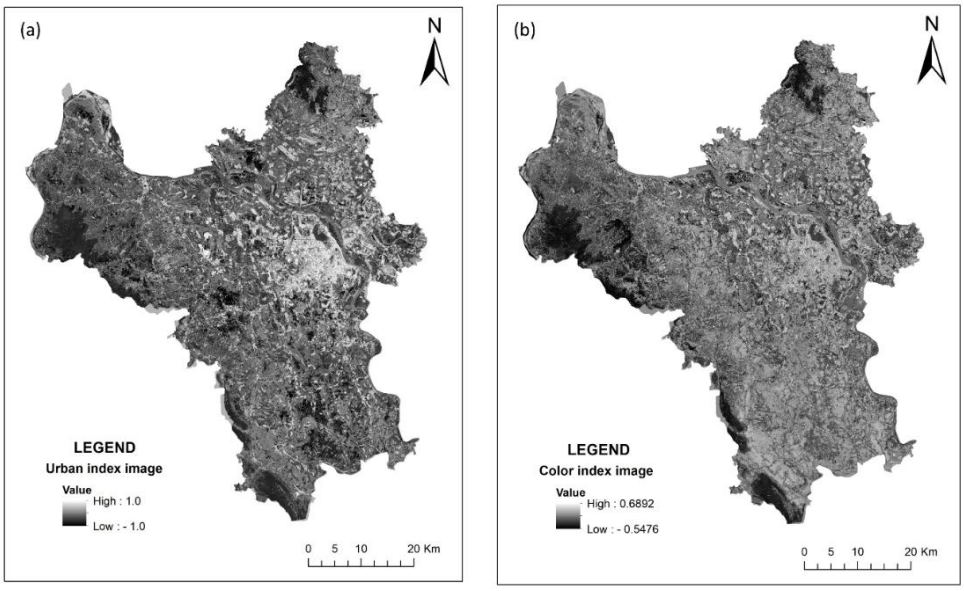


Figure 5. The remote sensing indices by Sentinel-2 imagery. (a) UI; (b) CI.

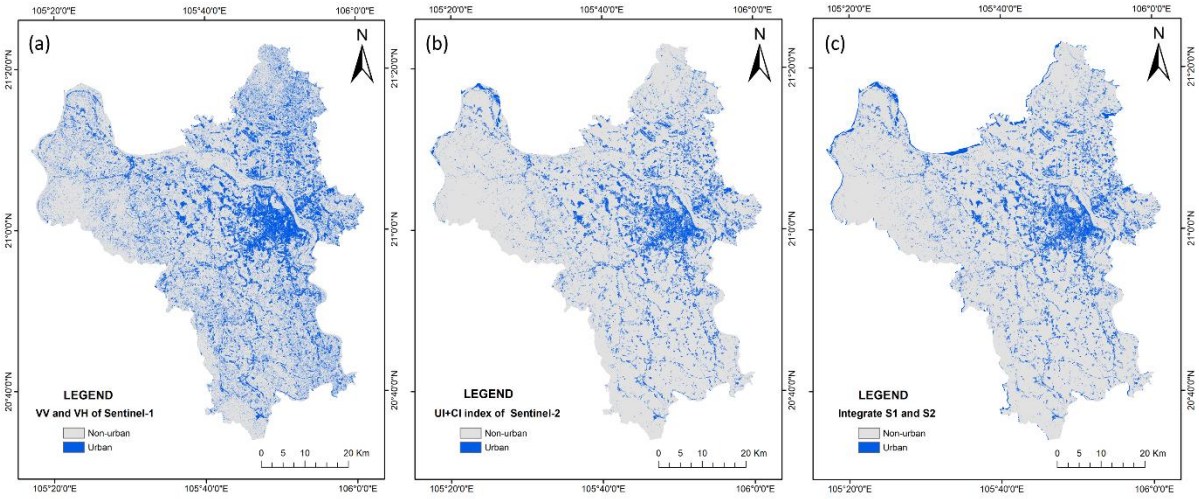


Figure 6. The classification results. (a) Scenario 1; (b) Scenario 2; (c) Scenario.

3 4. The Results and Discussion

To extract urban features in Hanoi for the year 2019, the authors conducted experiments using the proposed method described in Figure 3. These experiments involved the integration of Sentinel-1 and Sentinel-2 imagery. The InSAR coherence maps derived from Sentinel-1 are presented in Figure 4, while the spectral soil index images UI, CI extracted from Sentinel-2 are shown in Figure 5.

To evaluate the performance of the proposed method, three different data combinations were tested for classifying urban and non-urban features:

- Scenario 1: Utilizes two input layers representing the coherence maps of VV and VH polarizations obtained from Sentinel-1 imagery (Figure 6a).

- Scenario 2: Employs two spectral indices UI and CI derived from Sentinel-2 imagery (Figure 6b).

- Scenario 3: Integrates four bands, including the VV and VH coherence maps from Sentinel-1 and the two spectral indices (UI, CI) from Sentinel-2 (Figure 6c).

To evaluate the accuracy, the authors used 292 non-urban/urban checkpoints spread over the entire experimental area. Table 2 displays the results of the classification accuracy assessment.

Table 2. Classification accuracy assessment results

Metric	Scenario 1 *(S1 only)*	Scenario 2 *(S2 only)*	Scenario 3 *(S1 + S2)*
Overall accuracy	78.8%	88%	92.1%
Kappa index	0.556	0.744	0.829

According to the accuracy evaluation results in Table 2, the highest overall accuracy of 92.1%, with a corresponding Kappa index of 0.829, is obtained by integrating Sentinel-1 and Sentinel-2 data. The research results also indicate that the InSAR coherence map of VV and VH from Sentinel-1 image data is less accurate than using Sentinel-2 optical images to classify urban land objects. An InSAR coherence map using Sentinel-1 data with two polarizations, VV and VH, is used to classify urban features. The accuracy is over 78.8%, and the corresponding Kappa index is 0.556. The urban areas are accurately identified with high coherence values. However, due to the speckle noise on the SAR images, the InSAR coherence results are not only urban features. In addition, flat surface objects such as runways and highways have low coherence values due to low backscattering signals, which means these objects are not detected in the VV or VH coherence images of Sentinel-1. In rural areas of

Vietnam, red tiles are often used, so they reflect strongly on the CI index image. Therefore, the combined UI and CI image allows for a satisfactory classification of urban and rural residential areas. However, some bare land areas also strongly reflect the CI index image. Thus, the combination of the InSAR coherence map and spectral index images allows for the elimination of bare land and vegetation features on the resulting image. Some locations are mistakenly classified as flat roads, dry fields, and sand in the middle of the river.

5. Conclusion

In conclusion, the method of integrating InSAR coherence images of the Sentinel-1 satellite and spectral soil index images of the Sentinel-2 satellite provides an accuracy of over 90%. In addition, the experimental results also demonstrate the ability to apply only dual-polarization coherence maps from the Sentinel-1 satellite or the spectral soil index of Sentinel-2 for classifying urban features with an accuracy of 78.8% and 88%, respectively. However, the classification results still have some mistakes due to the influence of speckle noise on Sentinel-1 images and spectral index characteristics on Sentinel-2 images. To improve the accuracy of remote sensing indicators in Earth surface monitoring, it is necessary to conduct experiments on the geological and social geographical characteristics of each area. In addition, in the article, the authors used the K-means unsupervised classification method to identify urban features for the required accuracy. The research results of the article also show the ability to automatically classify and apply unsupervised machine learning algorithms in detecting and updating changes of urban features from optical and microwave remote sensing images.

References

[1] Q. Weng, Remote Sensing of Impervious Surfaces in the Urban Areas: Requirements, Methods, and Trends, Remote Sensing of Environment, Vol. 117, 2012, pp. 34-49.

[2] OpenDevelopment Vietnam, Urbanization in Vietnam, https://vietnam.opendevelopmentmekong.net/vi/topics/urbanization-in-vietnam/, 2025 (accessed on: October 18th, 2025).

[3] Hanoi Statistics Office, Hanoi Statistical Yearbook 2019, Statistical Publishing House, Hanoi, 2019, pp. 25-26.

[4] Hanoi Statistics Office, Hanoi Statistical Yearbook 2024, Statistical Publishing House, Hanoi, 2024, pp. 29-30.

[5] E. Kuruoglu, J. Zerubia, Modeling SAR Images With a Generalization of The Rayleigh Distribution, IEEE Trans. Image Process., Vol. 13, No. 4, 2004, pp. 527-533.

[6] D. Hong, L. Gao, N. Yokoya, J. Yao, J. Chanussot, Q. Du, B. Zhang, More Diverse Means Better: Multimodal Deep Learning Meets Remote-Sensing Imagery Classification, IEEE Transactions on Geoscience and Remote Sensing, Vol. 59, No. 5, 2021, pp. 4340-4354.

[7] M. S. Wong, X. Zhu, S. Abbas, C.Y. T. Kwok, M. Wang, Optical Remote Sensing, in: Urban Informatics, Publishing Springer, Singapore, 2021, pp. 315-344.

[8] C. Toth, G. Jozkow, Remote Sensing Platforms and Sensors: A Survey, ISPRS J. Photogrammetry Remote Sens., Vol. 115, 2016, pp. 22-36.

[9] Z. Huang, M. Datcu, Z. Pan, B. Lei, Deep SAR-Net: Learning Objects from Signals, ISPRS J. Photogrammetry Remote Sens., Vol. 161, 2020, pp. 179-193.

[10] X. Zhang, S. Feng, C. Zhao, Z. Sun, S. Zhang, K. Ji, MGSFA-Net: Multi-Scale Global Scattering Feature Association Network for SAR Ship Target Recognition, IEEE J. Sel. Top. Appl. Earth Observ. Remote Sens., Vol. 17, 2024, pp. 4611-4625.

[11] J. Liu, M. Gong, K. Qin, P. Zhang, A Deep Convolutional Coupling Network for Change Detection Based on Heterogeneous Optical and Radar Images, IEEE Trans. Neural Netw. Learn. Syst., Vol. 29, No. 3, 2018, pp. 545-559.

[12] J. Ling, H. Zhang, WCDL: A Weighted Cloud Dictionary Learning Method for Fusing Cloud-Contaminated Optical and SAR Images, IEEE J. Sel. Topics Appl. Earth Observ. Remote Sens., Vol. 16, 2023, pp. 2931-2941.

[13] Z. Du, X. Li, J. Miao, Y. Huang, H. Shen, L. Zhang, Concatenated Deep Learning Framework for Multi-Task Change Detection of Optical and SAR

Images, IEEE J. Sel. Topics Appl. Earth Observ. Remote Sens., Vol. 17, 2024, pp. 719–731.

[14] M. Schmitt, X. X. Zhu, Data Fusion and Remote Sensing: An Evergrowing Relationship, IEEE Geosci. Remote Sens. Mag., Vol. 4, No. 4, 2016, pp. 6-23.

[15] T. Baltrusaitis, C. Ahuja, L.-P. Morency, Multimodal Machine Learning: A Survey and Taxonomy, IEEE Trans. Pattern Anal. Mach.Intell., Vol. 41, No. 2, 2019, pp. 423-443.

[16] J. Hu, D. Hong, X. X. Zhu, MIMA: MAPPER-Induced Manifold Alignment for Semi-Supervised Fusion of Optical Image and Polarimetric SAR Data, IEEE Trans. Geosci. Remote Sens., Vol. 57, No. 11, 2019, pp. 9025-9040.

[17] Y. Sun, L. Lei, Z. Li, G. Kuang, Similarity and Dissimilarity Relationships Based Graphs for Multimodal Change Detection, ISPRS J. Photogrammetry Remote Sens., Vol. 208, 2024, pp. 70–88.

[18] Y. Sun, L. Lei, X. Li, X. Tan, G. Kuang, Structure Consistency-Based Graph for Unsupervised Change Detection with Homogeneous and Heterogeneous Remote Sensing Images, IEEE Trans. Geosci. Remote Sens., Vol. 60, 2022, pp. 1-21.

[19] Map Library, Data Analysis/Data Processing, https://www.maplibrary.org/1487/advanced-methods-for-integrating-satellite-imagery/, 2025 (accessed on: December 9th, 2025).

[20] T. Blaschke, Object Based Image Analysis for Remote Sensing, ISPRS Journal of Photogrammetry and Remote Sensing, Vol. 65, No. 1, 2010, pp. 2-16.

[21] N. V. Thinh, D. T. M. D. Minh, V. V. Phai, P. H. Hai, Hanoi Geography, Hanoi Pubulishing House, Hanoi, 2019 (in Vietnamese).

[22] D. V. Bao, Hanoi Rivers and Lakes, Hanoi Publishing House, Hanoi, 2019 (in Vietnamese).

[23] G. K. Trung, N. D. Vinh, T. D. Men, Soil Classification and Seismic Site Response Analysis for Some Areas in Hanoi City, VNU Journal of Science: Earth and Environmental Sciences, Vol. 34, No. 1, 2018, pp. 37-44, https://doi.org/10.25073/2588-1094/vnuees.4185.

[24] Home, News, Sentinel-1A Change in the Orbit Control Strategy, https://sentinels.copernicus.eu/-/sentinel-1a-change-in-the-orbit-control-strategy, 2025 (accessed on: December 9th, 2025).

[25] SentiWiki, Sentinel-1, S1 Mission, Overview of Sentinel-1 Mission, https://sentiwiki.copernicus.eu/web/s1-mission, 2025 (accessed on: December 9th, 2025).

[26] M. Joao, S. Marcus, F. Gianfranco, L. Riccardo, X-SAR Interferometry: First Results, IEEE Trans. Geosci. Remote Sens., Vol. 33, No. 4, 1995, pp. 950-956.

[27] H. Zebker, J. Villasenor, Decorrelation in Interferometric Radar Echoes, IEEE Trans. Geosci. Remote Sens., Vol. 30, No. 5, 1992, pp. 950-959.

[28] M. Preiss, A. Gray, N. J. S. Stacy, Detecting Scene Changes Using Synthetic Aperture Radar Interferometry, IEEE Trans. on Geosci. Remote Sens., Vol. 44, No. 8, 2006, pp. 2041–2054.

[29] H. Zebker, K. Chen, Accurate Estimation of Correlation in InSAR Observations, IEEE Geosci. Remote Sens. Lett., Vol. 2, No. 2, 2005, pp. 124-127.

[30] European Space Agency (ESA), Sentinel-2 Mission, Copernicus Open Access Hub Documentation. Available at: Sentinel-2 | Copernicus Data Space Ecosystem, 2025 (accessed on: October 19th, 2025).

[31] Y. Zha, J. Gao, S. Ni, Use of Normalized Difference Built-up Index in Automatically Mapping Urban Areas from TM Imagery, Int. J. Remote Sens., Vol. 24, 2003, pp. 583–594.

[32] M. Pouget, J. Madeira, E. L. Floch, S. Kamal, Spectral Characteristics of Sandy Surfaces in The North-Western Coastal Region of Egypt: Application to SPOT Satellite Data, Journee de teledetection, Vol. 12, 1991, pp. 27-39.